Journal of Electronic Materials
https://doi.org/10.1007/s11664-022-10130-x

ORIGINAL RESEARCH ARTICLE

The Combination of Nickel Oxide (NiO) and Molybdenum Trioxide (MoO_3) for Pollutant Gas Detection

Dharma K. Halwar[1] · **Vikas V. Deshmane**[2] · **Arun V. Patil**[3]

Received: 21 May 2022 / Accepted: 28 November 2022

Abstract

The prime objective of the current research was to analyze and utilize the coexistence of basic and acidic metal oxide semiconductors (MOS) for sensing pollutant gases. In the current work, 1 wt.%, 3 wt.%, 5 wt.%, 7 wt.%, and 9 wt.% NiO (basic MOS) was added to MoO_3 (acidic MOS), and thick films were prepared using the screen printing technique. Structural characterization was performed by x-ray diffraction (XRD), scanning electron microscopy (SEM), and energy-dispersive x-ray analysis (EDAX). The crystallite size was about 50 nm, with intermediate voids. EDAX analysis confirmed the non-stoichiometric composition of the films. The films were oxygen-deficient as per EDAX data. An electrical analysis involving resistivity, temperature coefficient of resistance (TCR), and activation energy was also performed. NiO3 samples showed maximum resistivity of 103.13×10^4 Ω·m and minimum activation energy of 0.3953 eV. The electrical analysis predicted the distinct behavior of the NiO3 sample. A negative TCR value indicated the semiconductor-like behavior of the samples. The pollutant gas response of the samples was analyzed using a static gas sensing apparatus. NiO3 samples showed gas sensitivity of 87% towards the ethanol vapors, with good selectivity, as compared with the responses towards CO, liquid petroleum gas (LPG), NH_3, and NO_2 gases. The oxygen vacancy-based gas sensing mechanism was the probable reason for the improved ethanol vapor sensing. The response time of the sample was 28 s, while the recovery time was 38 s.

Graphical Abstract

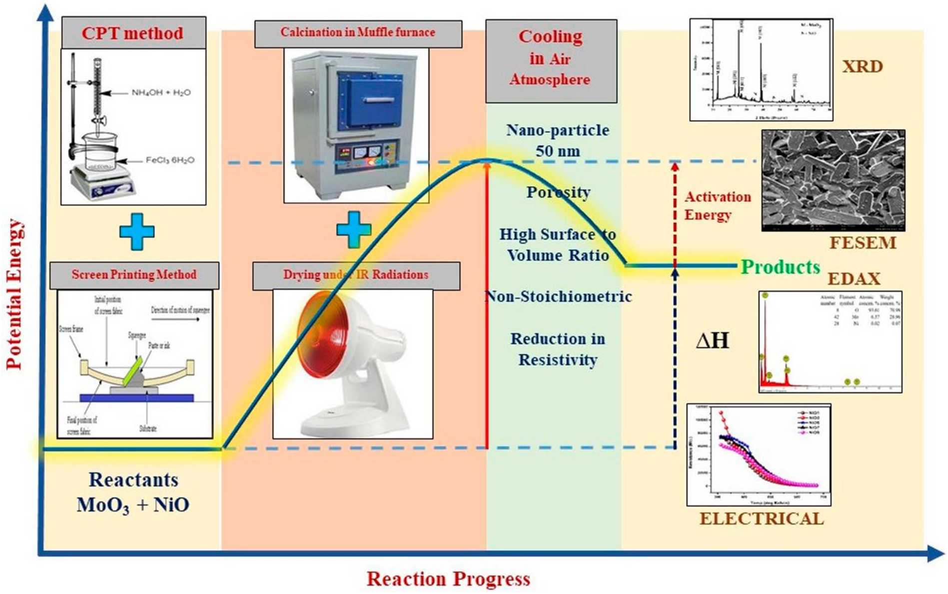

Keywords Molybdenum trioxide · nickel oxide · ethanol · oxygen vacancy · gas sensitivity · response time

---

Extended author information available on the last page of the article

Introduction

Volatile organic compounds (VOC) and hazardous gases are emitted into the air every day, causing pollution. As the number of vehicles and industries increases, the amount of VOC in the air is increasing drastically. Thus, monitoring and control of the air quality index has become the need of the hour. Good-quality and affordable gas sensors are in great demand today. The role of metal oxide semiconductors (MOS) has been studied for many years, and n-type and p-type MOS perform as gas sensors for various types of hazardous gases.

The role of molybdenum trioxide as a catalyst has been greatly acclaimed by the industry. Molybdenum trioxide (MoO_3) possesses a characteristic layered structure, with octahedral layers incorporated into the orthorhombic structure. Coupling between Mo (VI) and Mo (V) is easy in MoO_3. MoO_3 has a typical acidic character.[1] There have been relatively few studies of MoO_3-based gas sensors to date. The gas sensing properties of pristine MoO_3 can be greatly improved using proper additives.

Nickel oxide is a basic metal oxide. The nickel metal interacts with oxygen to form nickel oxide (NiO). Ni^{2+} and O^{2-} occupy the octahedral sites within the structure of NiO. NiO has also been reported as an efficient material for hole transport in solar cell applications.[2] NiO has a partially filled 3d band. Hence, it can serve as a good conductor and modify the properties of the MoO_3.[3] The basic nature of NiO and the valence electron make it a potentially good additive to improve the electrical and gas sensing behavior of the base material MoO_3.

The current study reports the effect of the addition of basic MOS (NiO) to acidic MOS (MoO_3). The thick films of the combinations were prepared using the screen printing method. The structural, electrical, and gas sensing properties of these thick films were studied. This combination performed as an excellent ethanol gas sensor.

Materials and Methods

The ratio of inorganic to organic materials used for the fabrication of undoped and doped MoO_3 thick film samples was 70:30. In inorganic materials, a commercial analytical reagent-grade powder of MoO_3 (99.9% pure, Merck) was used as a functional material. The MoO_3 powder was calcined in an air atmosphere in a muffle furnace (Therelek, 0–1200°C) for 1 h at 400°C. The ratio of active MoO_3 powder to permanent binder was kept at 95:5 in the 70% part. The permanent binder used was a glass frit (70 wt.% PbO, 18 wt.% Al_2O_3, 9 wt.% SiO_2, and 3 wt.% B_2O_3).[1–3] The organic part consisted of a temporary binder of 8% ethyl cellulose (Vishal-Chem, Mumbai, India) and 92% butyl carbitol acetate (Vishal-Chem, Mumbai, India; $C_{10}H_{20}O_4$, BP 245°C) as a vehicle for making the paste. To obtain the desired viscosity and thixotropic properties of the paste, butyl carbitol acetate was added dropwise to the powder mixture. In addition, 1 wt.%, 3 wt.%, 5 wt.%, 7 wt.%, and 9 wt.% NiO (an additive) and 99 wt.%, 97 wt.%, 95 wt.%, 93, and 91 wt.% MoO_3 (as base material) were mixed. The prepared films of 1, 3, 5, 7, and 9 wt.% NiO are referred to as NiO1, NiO3, NiO5, NiO7, and NiO9, respectively. These combinations were used to prepare thick films on glass substrates using the screen printing method. The films were exposed to IR radiation for 15 min. These films were fired at 600°C in a muffle furnace. The thick films were characterized using various characterization techniques. The selected target species contains hazardous gases as well as certain volatile compounds. The selected target gases are those most commonly liberated in daily life, such as ammonia (from animal husbandry and ammonia-based fertilizers), nitrogen dioxide, and carbon monoxide (from vehicle exhaust). The household leakage of liquid petroleum gas (LPG) is a well-known problem nowadays. The use of ethanol as biofuel has also increased ethanol-based pollution. Hence, the common day-to-day pollutants were selected for the study.

As shown in Fig. 1, the dimensions of the rectangular films were 25 mm × 12.5 mm. The mass of the substrate before and the total mass of the prepared films were used to calculate the actual mass of the material deposited. The density of the material was used to calculate the thickness of the films (15–20 µm).

The structural properties of the prepared thick films were studied using x-ray diffraction (XRD) (Bruker D8 Advance), field emission scanning electron microscopy (FESEM) (JEOL 6300 (LA), Germany), and energy-dispersive spectroscopy (EDAX).

A static gas sensing apparatus (Fig. 1) was used to analyze the electrical and gas sensing properties of the films. The setup consists of a series of combinations of resistance (2 MΩ), and the films to be tested are placed inside a 21 L sealed glass chamber. A DC power supply (0–30 V) was connected across the series combination. The changes in the resistance of the film were recorded with a microvoltmeter. The change in the chemical surroundings of the sample was quantified as the sample resistance. The changes in resistance of the films in the presence of the target gas were termed the "relative response" against the particular target gas. The temperature inside the chamber was recorded using a thermocouple. The target gas was not sprayed directly on the surface of the film but released in the sample environment. This method is closer to real-life gas exposure.

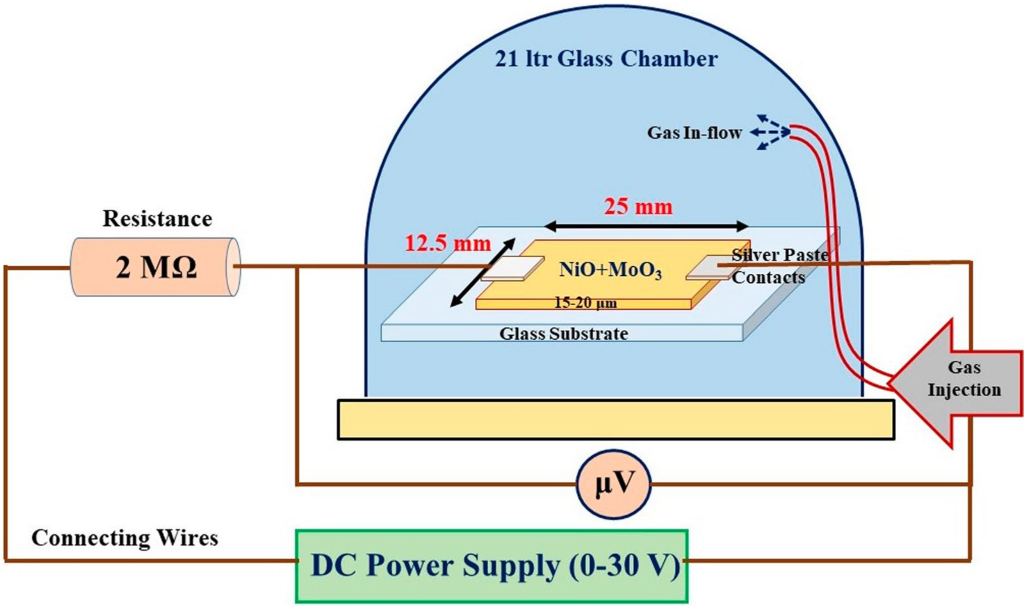

Fig. 1 Schematic of setup for electrical analysis and static gas sensing studies.

Results and Discussion

Drying and Firing of the Films

The heat treatment of thick films plays an important role in determining their structural and surface properties. After preparation, the films were exposed to infrared (IR) rays. This radiation generated heat, causing the evaporation of the temporary binders.[4] Further, the films were kept in the furnace for about 1 h in an air atmosphere. In this process, a constant temperature of 600°C was maintained. The glass frit, which was mixed as a permanent binder, softens at 600°C. The adherence of the material to the alumina substrate is improved during this procedure.

Structural Characterization (X-ray Diffraction Study of MoO_3: NiO Thick Films)

The structural properties of MoO_3 and NiO are modified due to the heat treatment at 600°C. The structural properties of the thick films were studied using XRD, FESEM, and EDAX. Key parameters such as crystallite size, structure, and phase can be determined using x-ray diffraction.[5] The x-rays of Cu-K_α radiation were used in the range of 20°–80°.

The diffraction peaks at 2 theta positions 12.9°, 23.3°, 25.6°, 27.7°, 39.0°, 39.9°, and 59.2° correspond to the [001], [101], [002], [011], [102], [103], and [122] planes of the samples that perfectly matched the JCPDS 47-1320 (Fig. 2). The XRD data confirmed that the base material used is MoO_3. The minor peaks at positions 35.6°, 46.6°, and 63.447° correspond to the nickel oxide (NiO) according to the JCPDS no. 73-1523.

The diffraction peak located at 25.64° had the highest intensity among all peaks. Hence, [002] was the preferred plane of the MoO_3. The intensity variations showed that the material was crystalline. The anisotropic growth of the crystal is reflected in the intensity of the peaks. The broadening of the XRD peaks can be attributed to the misfits and defects in the crystal. The heterojunction between MoO_3 and NiO play a role in the broadening of the XRD peaks.[5]

The Debye–Scherer formula was used to calculate the crystallite size. This formula uses the wavelength of x-rays (λ), angle of incidence (θ), and full width at half maximum (β) of the diffraction peak.[6]

$$D = 0.9\lambda/\beta\cos\theta \tag{1}$$

The changes in average crystallite size with the wt.% of NiO are shown in Table I. The peak analysis was carried out using XPowder 12 software (ver. 2014.04.34). The sample peak analysis is shown in Fig. 3. All of the crystallites had a size in the nanometer range. The NiO3 thick films had the lowest average crystallite size among the thick film samples. The minimum crystallite size corresponds to the maximum surface-to-volume ratio of the crystallites. The increased surface-to-volume ratio facilitates gas adsorption. The higher gas adsorption causes better gas sensitivity.[7]

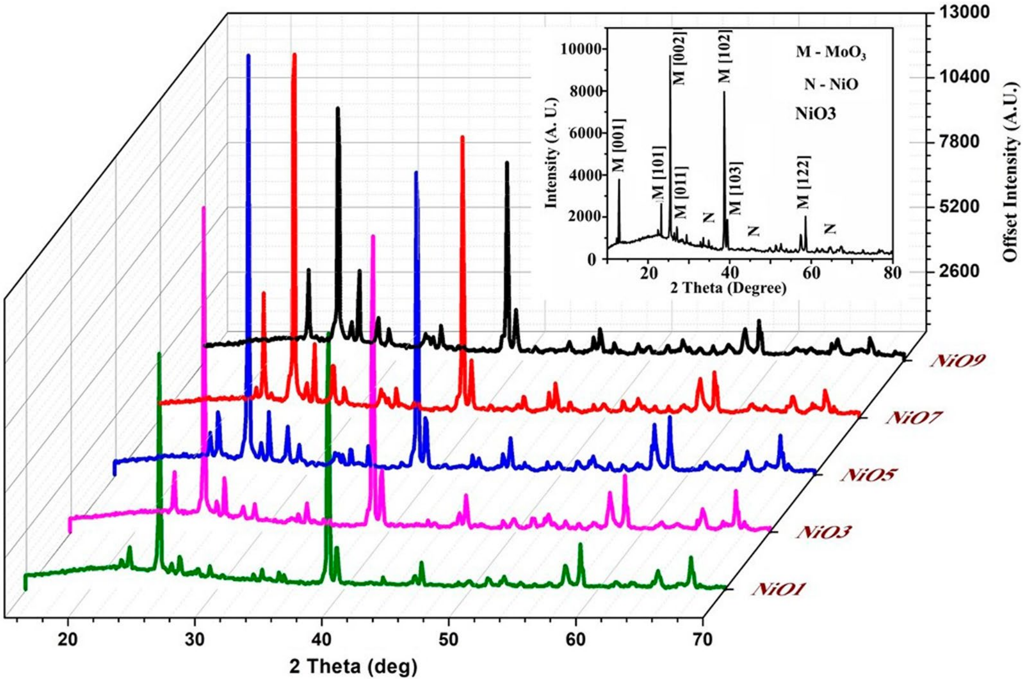

Fig. 2 X-ray diffraction patterns of NiO1, NiO3, NiO5, NiO7, and NiO9 thick films, Inset: XRD peaks of NiO3 as a representative.

Table I The average crystallite size for the NiO1, NiO3, NiO5, NiO7, and NiO9 thick films

NiO wt.%	Average crystallite size (nm)
1	54
3	42
5	47
7	56
9	49

SEM Analysis of MoO$_3$: NiO Thick Films

The morphology and texture of the surface of the thick films have a major role in the surface-related interaction. The surface reaction in turn influences the internal movement of the charge carriers. Scanning electron microscopy (SEM) of the prepared thick films was carried out using a JOEL 6365 (Germany) instrument (Fig. 4). Before the actual SEM, the thick films were coated with a very fine layer of gold. This layer prevents the charging of the surface of the thick film and results in excellent micrographs.

The micrographs showed that with the addition of nickel oxide (NiO), the length and width of the MoO$_3$ lamellar structure were reduced. For 1 wt.% NiO, the plank-like layers of MoO$_3$ are distinct and lengthy. As the weight percent of the NiO additive increases, more of the additive is found residing on the surface of the lamina. For the thick films with 7 wt.% and 9 wt.% of additive, the lamellar structure was almost covered by the additive. For 9 wt.% NiO, the length and width of MoO$_3$ lamellar structure were found to be shortened.

The formation of long layers was hampered due to the presence of the additive. During the firing process, the nickel oxide additive may disturb the long-range ordering of the MoO$_3$ layers. The inclusion of additives might have broken the layered continuity and hence caused a reduction in dimensions.[8] Interlayer gaps were also observed on the surface of the thick films, and porosity of the films was observed. This surface morphology favors the adsorption of target gases and hence improves gas sensitivity.

EDAX: Energy-Dispersive X-ray Analysis

The weight percentage and atomic percentage of the elements in the thick film material were investigated using energy-dispersive spectroscopy. A JEOL 6365 (Germany) instrument was utilized for this purpose. Figure 6f shows the representative EDAX spectra of the NiO1 films.

The data retrieved from the EDAX analysis are summarized in Table II. The EDAX data confirmed the presence of molybdenum (Mo), oxygen (O), and nickel (Ni) in the thick films. The Mo:O proportion was changed to an additive weight percent. It appeared from the atomic percentage data that the weight percent of additive increased and oxygen was liberated. The NiO additive clearly modified the constituents of the thick films. The change in oxygen content

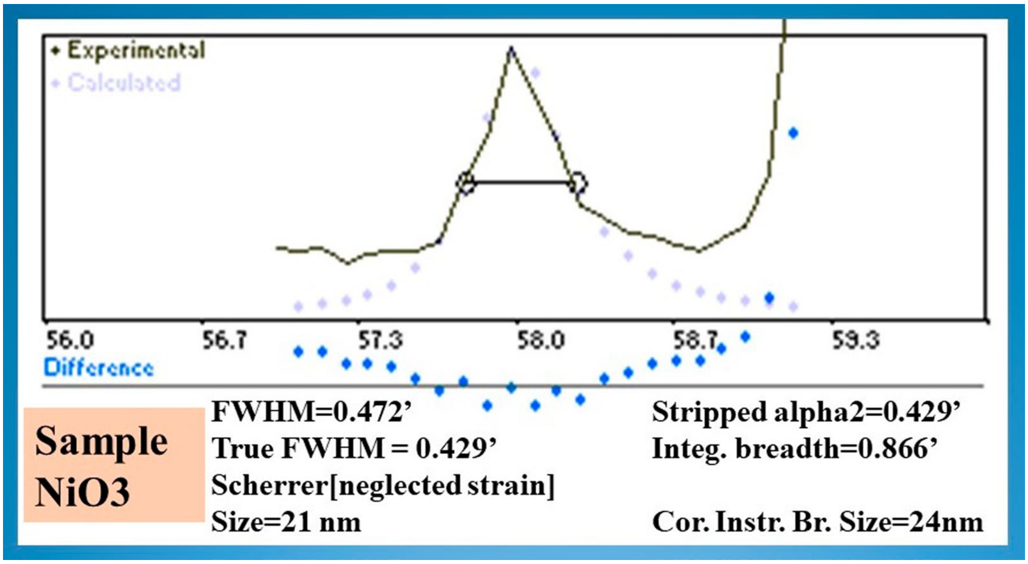

FWHM=0.472’
True FWHM = 0.429’
Scherrer[neglected strain]
Size=21 nm
Stripped alpha2=0.429’
Integ. breadth=0.866’
Cor. Instr. Br. Size=24nm

Fig. 3 Peaks of a NiO3 sample analyzed using XPowder 12 software (ver. 2014.04.37).

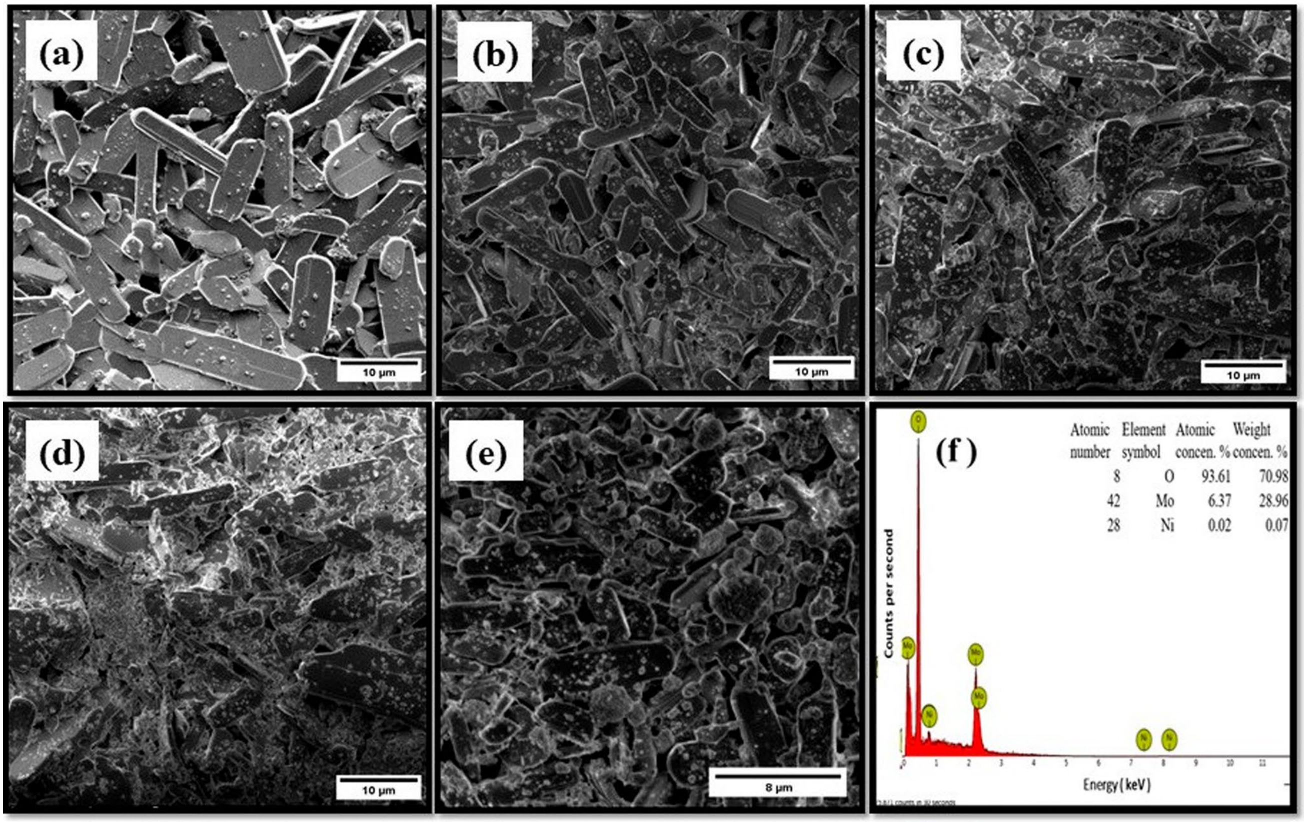

Atomic number	Element symbol	Atomic concen. %	Weight concen. %
8	O	93.61	70.98
42	Mo	6.37	28.96
28	Ni	0.02	0.07

Fig. 4 (a-e) FESEM micrographs of 1 wt.%, 3 wt.%, 5 wt.%, 7 wt.%, wt.% and 9 wt.% NiO-doped MoO_3 thick films, (f) EDAX spectra for NiO1 sample.

also plays an important role in conductivity and gas sensing mechanisms.

The desirable molybdenum (Mo) to oxygen (O) proportion is 1:3. But the EDAX data shows non-stoichiometry in the elemental concentration. The deficiency or excess of oxygen changes the band structure of the neutral base material. The adsorbed or liberated oxygen traps or releases two electrons per atom. The oxygen association modifies the number of free charge carriers, and hence the conductivity of the thick films is altered.[9]

Table II Composition of NiO1, NiO3, NiO5, NiO7, and NiO9 thick films.

Element	Weight concentration				
	1 wt.%	3 wt.%	5 wt.%	7 wt.%	9 wt.%
O	71.00	63.30	57.17	54.72	52.06
Mo	28.94	36.61	41.73	43.98	46.54
Ni	0.06	0.09	1.10	1.30	1.44

Electrical Characterization

The electrical properties of thick films were studied using a simple potential divider arrangement. The arrangement had a series combination of standard resistance and thick films to be studied. The whole assembly was kept in a chamber, whose temperatures were maintained using the heater. The temperature was increased in steps of 10°C, and the corresponding DC resistance of the sample was calculated. The changes in thick film resistance with increasing temperatures of NiO1, NiO3, NiO5, NiO7, and NiO9 thick films are shown in Fig. 5a.

The DC resistance of the thick films first decreased linearly with increasing temperature. Then, in a second region, the resistance decreased exponentially with the increase in temperature. For the higher temperatures, the resistance almost saturated to the lowest value of the resistance of the thick films. The thick films showed n-type semiconducting behavior.[10] The values of the temperature coefficient of resistance were also found to be negative.

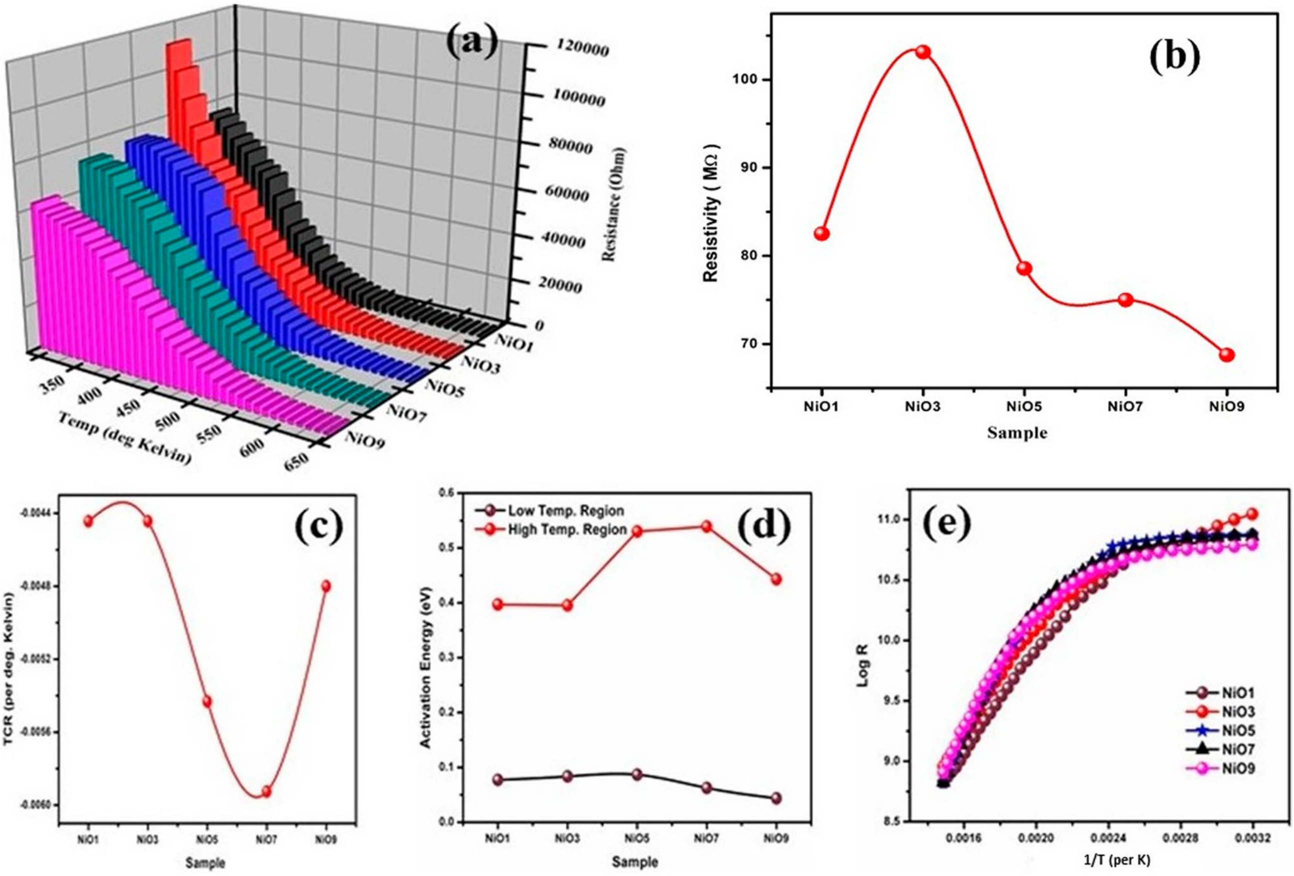

Fig. 5 Variation in (a) resistance with temperature, (b) resistivity, (c) TCR, (d) log(R) versus 1/T, and (e) activation energy in the low- and high-temperature regions for NiO1, NiO3, NiO5, NiO7, and NiO9 thick films fired at 600°C.

Resistivity of MoO_3: NiO Thick Films

The resistivity of the thick films was calculated using the resistance (R), length (l), breadth (b), and width (t) of the thick film samples, using the following formula.[11]

$$\rho = (R \times b \times t)/l \qquad \Omega.m \tag{2}$$

The thickness of the films was calculated using the standard density formula. The films were printed on an alumina substrate in a 1.25 cm × 2.5 cm area. The mass of the material was calculated using pre- and post-preparation mass measurements. The thickness of this rectangular thick film was found to be about 15–20 microns.

The resistivity increased slightly with the addition of NiO. The resistivity was greatest (103×10^4 Ω·m) for the NiO3 thick films (Fig. 5b) and was found to decrease with a further increase in NiO weight percent as compared with NiO3 (Table III).

The barriers formed at the boundaries between NiO and MoO_3 can be used to explain the current resistivity behavior of thick films. The inclusion of NiO might create interstitial defects in the MoO_3 base material. These generated defects form the depletion layers, which lead to potential barrier formation.[12] The ionic radius of Mo^{6+} is 0.62 Å, whereas the ionic radius of Ni^{2+} is 0.72 Å.[13] These ionic radii are comparable, and hence Ni^{2+} can occupy the interstitial positions. The difference between the oxidation states of nickel and molybdenum will introduce defects within the structure of the thick film material. Oxygen vacancies may be introduced within the structure. Hence, the resistivity of the sample is modified.[14]

The summary of electrical parameters of resistivity, TCR, and activation energy in high- and low-temperature regions is presented in Table III.

TCR of MoO_3: NiO Thick Films

The variation in resistance with temperature can occur in two ways. If the resistance of the semiconductor increases with an increase in temperature, then this type of material is said to have a positive temperature coefficient. In another type, the resistance of the sample may decrease with an increase in temperature, and such material is supposed to have a negative temperature coefficient.

Table III Resistivity, TCR, and activation energy for NiO1, NiO3, NiO5, NiO7, and NiO9 thick films

Sample	Resistivity × 10^4 (Ω·m)	TCR (/°K)	Activation energy (eV)	
			Low-Temp. Region	High-Temp. Region
NiO1	82.51	−0.0044	0.077	0.397
NiO3	103.13	−0.0044	0.084	0.395
NiO5	78.57	−0.0054	0.087	0.531
NiO7	74.99	−0.0059	0.063	0.539
NiO9	68.75	−0.0048	0.044	0.443

The temperature coefficient of resistance (TCR) can be calculated using room-temperature resistance (R_o), change in resistance (ΔR), and the corresponding temperature change (ΔT). The formula used to calculate TCR was as follows:[15]

$$TCR = \frac{1}{R_o}\left(\frac{\Delta R}{\Delta T}\right) \ /^{O}K \tag{3}$$

Figure 5c demonstrates the changes in TCR with the weight percent of NiO additive. All of the thick films exhibited a negative TCR. This is characteristic of the n-type semiconductor. Hence it can be observed that the molybdenum trioxide behaved like an n-type semiconductor despite the presence of the NiO additive.

Activation Energy of MoO_3: NiO Thick Films

Arrhenius plots play an important role in understanding the electrical behavior of thick films. They comprise a graph of the logarithm of resistance versus the inverse of the temperature of the thick film sample. Figure 5d shows the Arrhenius plot for the NiO1, NiO3, NiO5, NiO7, and NiO9 thick films.

The Arrhenius plot had two clear regions: a high-temperature region and a low-temperature region. In the high-temperature region, the region increases linearly with a nearly constant slope. In the low-temperature region, the slope of the graph becomes very small, i.e., saturation. The point that connects the two regions is called the transition point, and the corresponding temperature is called the transition temperature. The transition temperature is the temperature around which the behavior of the thick film sample changes from an active to a relatively inactive form. It can be concluded that relatively large changes in resistance can be observed in high-temperature regions. This fact is obvious since at higher temperatures the supplied heat energy is larger. As the supply of heat energy increases, the changes are inevitable.[16]

The activation energies in the high- and low-temperature regions can be calculated using the Arrhenius equation.

$$R = Ro\ e^{-\Delta E/KT} \tag{4}$$

here R is the resistance of the film at temperature T, R_o is the room-temperature resistance, ΔE is the activation energy, and K is the Boltzmann constant.[17]

The amount of energy required for an electron to jump from the valence band to the conduction band is the activation energy of the electron. The changes in activation energy in the high- and low-temperature region with the weight percentage of the additive are shown in Table III. The activation energy in the low-temperature region was very low, as observed in Fig. 5e. The activation energy in the high-temperature region was relatively higher as compared with the low-temperature region. The activation energy was found to be lowest (0.39 eV) for NiO1 and NiO3 thick films. The NiO5 and NiO7 thick films had higher activation energies (0.53 eV).[18]

Sample-to-Sample Variation

The abovementioned characteristics in Table III are the average of the characteristics of three samples for each weight percent of the additive. The sample-to-sample variation in the electrical properties indicates the repeatability of the results. Table IV summarizes the sample-to-sample variations in the resistivity, TCR, and activation energy of NiO1, NiO3, NiO5, NiO7, and NiO9 thick films.

Gas Sensing Analysis

The gas sensing properties of the prepared thick films were studied using a static gas sensing apparatus. The apparatus was based on the principle of a chemiresistive sensor. The current flowing through the circuit of the thick films is changed in the presence of the target gas due to the interaction between the target gas and the materials of the thick films.

The temperature of the surrounding thick films was varied in steps of 50°C, and corresponding changes in current were measured. Ohm's law was used to correspond with changes in film resistance. A total of 1000 ppm of target gases, namely CO, LPG, NO_2, NH_3, and ethanol vapor, were injected into the surrounding thick films. The changes in resistance were used to calculate the sensitivity of thick films toward the gas as per the following equation:

$$\text{Sensitivity}(S) = \left| \frac{R_a - R_g}{R_a} \right| \times 100 \tag{5}$$

where R_a is the resistance of the thick films in the presence of the air atmosphere, and R_g is the resistance of the thick films in the gas atmosphere.[19]

Optimization of the Operating Temperature and Sensitivity of Gas Sensor

Based on the activation energy studies, the maximum gas sensitivity temperatures would be in the high-temperature region. The optimal operating temperature is the one at which the thick films show maximum gas sensitivity. At the optimum temperature, the amount of supplied thermal energy is just sufficient for an electron to jump from the conduction band to the valence band.

Figure 6a-e indicates the gas sensing properties of NiO1, NiO3, NiO5, NiO7, and NiO9 thick films fired at 600°C. The optimum gas sensing temperature was nearly 250°C for the thick film samples. The NiO3 thick films showed 87.12%

Table IV Electrical outcomes of NiO-added MoO_3-thick films

Films	Sample	Room-temperature resistivity × 10^4 (Ω·m)	TCR (/°K)	Activation energy (eV)	
				Low-temp. region	High-temp. region
NiO1	S_1	82.21	−0.00451	0.0789	0.412
	S_2	82.70	−0.00430	0.0754	0.386
	S_3	82.52	−0.00444	0.0772	0.397
NiO3	S_1	103.13	−0.00444	0.0835	0.395
	S_2	102.84	−0.00427	0.0822	0.401
	S_3	103.42	−0.00453	0.0841	0.392
NiO5	S_1	79.12	−0.00534	0.0872	0.551
	S_2	78.03	−0.00552	0.0855	0.499
	S_3	78.57	−0.00543	0.0866	0.530
NiO7	S_1	74.99	−0.00593	0.0625	0.542
	S_2	74.67	−0.00605	0.0633	0.519
	S_3	75.29	−0.00588	0.0618	0.561
NiO9	S_1	68.84	−0.00494	0.0439	0.438
	S_2	68.75	−0.00481	0.0436	0.443
	S_3	68.67	−0.00470	0.0432	0.449

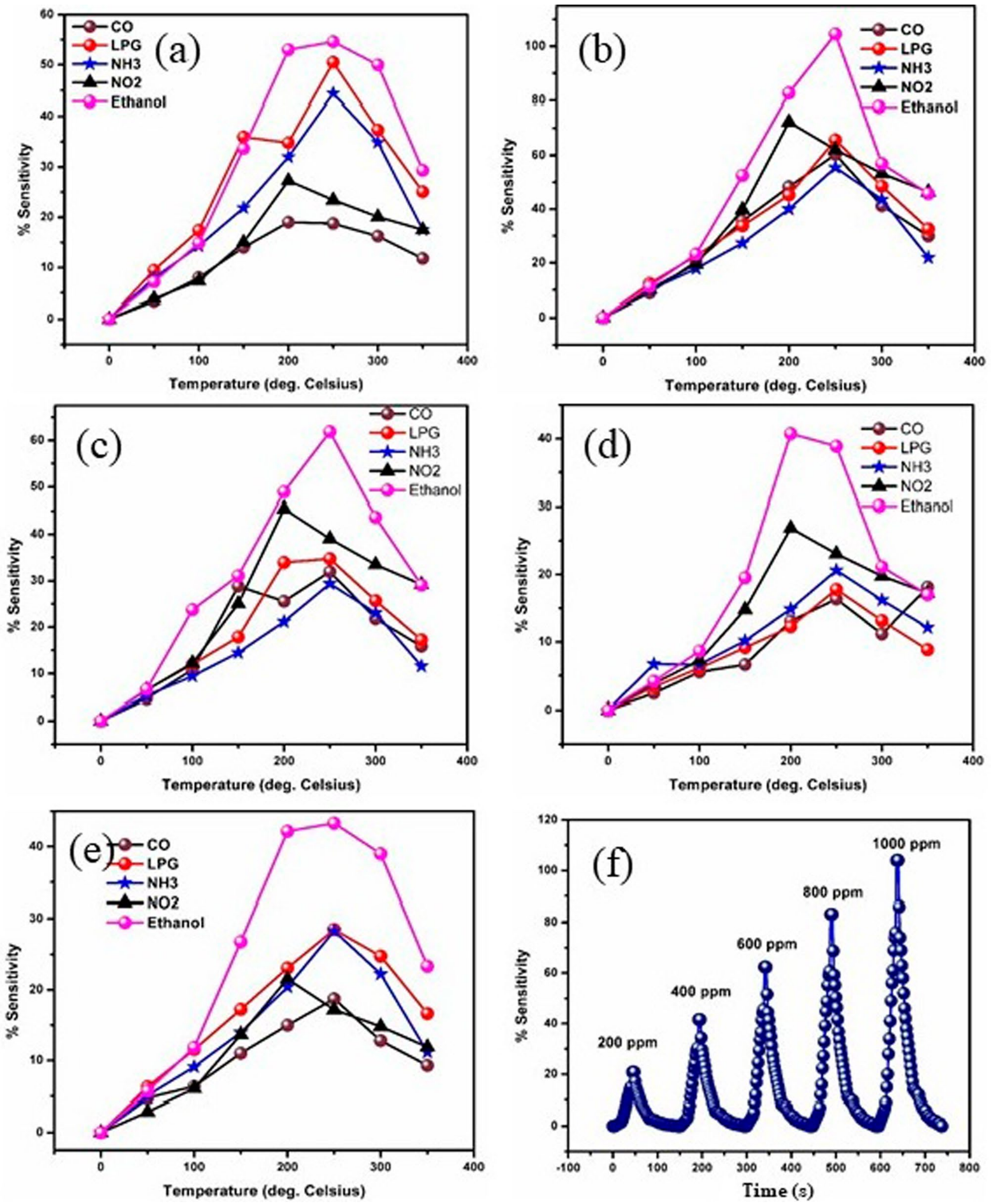

Fig. 6 Gas sensing properties of (a) NiO1, (b) NiO3, (c) NiO5, (d) NiO7, and (e) NiO9 thick films. (f) Percentage sensitivity versus ethanol vapor concentration for NiO3 thick films at a constant temperature of 250°C with time.

sensitivity to the ethanol vapor sensor at 250°C. The gas sensitivity increased gradually for lower temperatures up to 250°C and then decreased up to 350°C.

Ethanol Vapor Sensor

The hazardous effects of oral alcohol consumption have been known and studied for many decades. But the inhalation of alcohol vapors is significantly hazardous, as the vapors directly reach the arterial circulations. The vapors can even reach the brain, causing pharmacological effects.[20] Continuous exposure to ethyl alcohol vapors causes skin irritation.[21] Heated ethanol vapors can also injure the lungs.[22]

The gas sensing mechanism of the metal oxide semiconductors is based on the chemiresistive principle. The resistance of the thick films is affected by their exposure to the target gases. The oxidation and reduction mechanisms are one of the basic mechanisms that explain the changes during the gas sensing process. During the oxidation reaction, atmospheric oxygen is adsorbed on the film surface and attracts a nearby electron to cause a change in conductivity. During the reduction reaction, the lattice oxygen interacts with the target gas and completes the gas sensing process.[23–25]

The ionic radius of Mo^{6+} is 0.62 Å, whereas the ionic radius of Ni^{2+} is 0.72 Å.[14] These two radii are comparable. If Ni^{2+} is incorporated into the Mo^{6+} position to compensate for the valency difference, oxygen vacancies are generated. The below reaction represents the probable mechanism for oxygen vacancy formation. Here, $Ni^{''''Mo}$ is the nickel ion that replaces interstitial Mo. This nickel ion has four negative charges. O_{ox} is the oxygen present at the original lattice positions. $O^{\bullet\bullet v}$ is the oxygen vacancy formed during this process. The oxygen vacancy has double positive charges. These oxygen vacancies play a key role in the gas sensing mechanism.

$$\mathrm{NiO} \rightarrow \mathrm{Ni}^{''''\mathrm{Mo}} + \mathrm{O}^{\mathrm{ox}} + 2\mathrm{O}^{v} \tag{6}$$

For the MoO_6, the edge-linked system is preferred over the corner-linked system. Hence, the gas sensing mechanism in MoO_3 is driven by the lattice oxygens near the film surface. The catalytic oxidation of ethanol involves dehydration and hydrogenation processes. Molybdenum trioxide molecules with oxygen vacancies take part in the oxidation of ethanol vapors. The ethanol sensing mechanism can be explained using the following reactions:

$$\mathrm{C_2H_5OH(ads)} + 2\mathrm{O}^{v} \rightarrow \mathrm{CH_3CHO(ads)} + \mathrm{H_2O(ads)} + \mathrm{V}_2^{+o} + 2e^{-} \tag{7}$$

The same mechanism is shown in Fig. 7. The green portion of the figure indicates the depletion region that formed. During the intermediate processes, the adsorbed hydroxyl group desorbs as water. Acetaldehyde is formed as an intermediate product. This acetaldehyde oxidizes to form H_2O and CO_2. These liberated electrons cause a change in the conductivity of the thick films.[26–28]

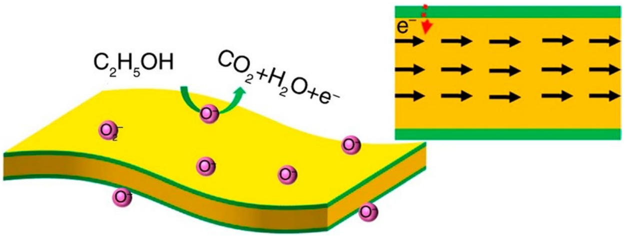

Fig. 7 Schematic of ethanol sensing [reprinted from reference 29, under the terms of the Creative Commons Attribution 4.0 International License (CC BY 4.0)] (Color figure online).

Table V Selectivity of NiO3 thick films to 1000 ppm CO, NH_3, LPG, NO_2, and ethanol vapors at 250°C

Target gas	Relative response	% Selectivity
CO	60.34	69.26
LPG	65.67	75.39
NH_3	55.49	63.69
NO_2	62.09	71.27
Ethanol vapors	87.12	100

Selectivity of Other Gases Against Ethanol

The selectivity of the gas sensor is a very important parameter. The sensitivity of the target gas (*S target gas*) and the sensitivity of other gas (*S other gas*) were used to calculate the percentage selectivity of the gas sensor. The percentage selectivity was calculated using the following formula:

$$\%\ \text{Selectivity} = \left(S_{\text{other gas}} / S_{\text{target gas}}\right) \times 100 \tag{8}$$

The percentage selectivity for CO, NH_3, LPG, NO_2, and ethanol vapors by NiO3 thick films is tabulated in Table V, which shows the percentage selectivity of NiO3 thick films to 1000 ppm of ethanol vapors at 250°C to carbon monoxide, ammonia, liquefied petroleum gas, nitrogen dioxide, and ethanol vapors. The maximum sensitivity offered against ethanol vapors was considered as 100%. The selectivity of other gases was calculated using this value as a reference (Table V).[29]

Variation in Sensitivity with Gas Concentration (ppm)

The changes in target gas concentration affect the gas sensing performance of the thick films. The NiO3 thick film sample was kept at a constant temperature of 250°C. The concentration of the ethanol vapors varied from 200, 400, 600, 800, to 1000 ppm. The corresponding changes in gas sensitivity were also noticed. This trend of sensitivity with the ethanol vapor concentration has been showcased in Fig. 6f.

It was observed that the sensitivity of the thick films to ethanol vapors increases linearly up to 600 ppm. After 600 ppm, the increase in sensitivity was relatively slower. These observations were quite obvious since at lower concentrations of ethanol vapor, the available target vapors were in smaller proportions. At these lower concentrations, a single molecular layer will be formed on the surface of the thick film, causing changes in the conductivity of the sample. As the ethanol vapor concentration increases, multiple layers of ethanol will be formed on the surface. The ethanol molecules away from the surface cannot interact with the surface, hence the relative increase in sensitivity was observed to be slower.[30]

Response Time and Recovery Time

The changes in sensitivity with time were also studied using a static gas sensing apparatus. The changes in sensitivity to 1000 ppm ethanol vapors with time are shown in Fig. 6f. The temperature was maintained at 250°C throughout the current observations. The response and recovery time are the key parameters for a good gas sensor. The response time is the time taken by the gas sensor to attain 90% of the maximum value of sensitivity. The quick recovery of the gas sensor is also crucial. The recovery time is the time taken by the gas sensor to decrease the sensitivity to 10% of its maximum value. According to the current study, the response time was found to be quick (28 s), whereas the recovery time was also quick (38 s). Hence, the NiO3-added MoO_3 thick

Table VI Comparison with recent heterostructure-based gas sensor reports

Material & heterostructure	Target gas & concentration (ppm)	Synthesis method	Optimum temp & gas response	Response & recovery time (s)	Particle size (nm)	Ref.
ZnO/NiO p-n	N-propanol 500	Bimetallic organic framework	275 280.2	31.5 18.2	10–34	31
NiO/Co_3O_4 p-p	VOC 50	Glancing angle deposition	350 1.6	–	–	32
NiO/CNT p-n	Acetone 40	Atomic layer deposition	200 –	–	21	33
$LaFeO_3$/NiO p-p	Ethanol 10	Hydrothermal	240 14.7	2 9	200–300	34
NiO/SnO_2 p-n	Ethanol 100	Co-precipitation and sol–gel	Room 140	23 13	–	35
Fe_2O_3/MoO_3 n–n	Xylene 100	Chemical	233.5 22.48	4 102	200–300	36
MoO_3/ZnO n–n	Ethanol 500	Hydrothermal	250 –	2.5 3.5	200–300	37
ZnO/NiO p-n	Hydrogen 100	Chemical	225 72	–	–	38
ZnO/NiO p-n	VOC 100	Transport and condensation	400 4	6.7 10	15–60	39
NiO/SnO_2 p-n	Formaldehyde 100	Hydrothermal	100–200 6.6 to 41.6	–	10–20	40
$NiGaO_4$/NiO p-p	Toluene 100	Solvothermal	230 12.7	–	34	41
NiO/ZnO n-p	Sulfur dioxide 20	Hydrothermal	240 16.25	52 41	39.71	42
CuO-NiO n-p	Glycol 100	One-pot synthesis	100 10.35	15 45	300	43
Fe_2O_3/NiO n-p	Acetone 100	Hydrothermal	280 290	28 40	156–178	44
NiO/MoS_2 p-n	Ammonia 20	Hydrothermal	Room 63	160 117	58.91	45
NiO/MoO_3 p-n	Ethanol 1000	Co-precipitation	250 87	28 38	50	Current Study

film behaved as a good ethanol vapor gas sensor with quick response. The repeatability of the results was also found to be excellent.[31–45]

Comparative Study

The outcomes of the current research work were compared with the recently published work on heterostructure-based gas sensors in 2018. The researchers have published work on various p-p, p-n, and n-n heterostructures for gas sensor applications. The comparison has been summarized in Table VI. The average particle size calculated in the current work was around 50 nm, which was good compared to the method of synthesis employed.

It was observed that the NiO and MoO_3-based heterostructures have not been studied for gas sensing applications. In this sense, the recent work is a novel attempt to understand the gas sensing response of the combination. The combination worked as a p-n type heterostructure. The current study also has the advantage of using a simple synthesis method (co-precipitation), which is easily reproducible and cost-effective. Current research work reports the optimum gas sensing temperature to be 250°C.

All the referenced reports used the sensitivity = R_a/R_g formula for calculation. The current study utilized sensitivity = Mod $[(R_a-R_g)/R_a]$; therefore, the response of 87% is quite good. The response and recovery time was excellent comparatively.

Pristine molybdenum trioxide and its combination with multiple metal oxides have been tested for gas sensing applications. Similarly, nickel oxide and its multiple combinations have also been analyzed for the same purpose. But the combination of molybdenum trioxide and nickel oxide in varying proportions has not been examined for gas sensing applications. The current study has implemented the simplest method of screen printing for the preparation of robust and sensitive chemiresistive gas sensors. The gas sensing result also had good repeatability. Certain parameters need improvement in the future. The concentration of the target gas used for analysis could be reduced below 100 ppm. The reduction in the optimum sensing temperature also remains a challenge.

Conclusion

Nickel oxide added to molybdenum trioxide showed an improved response to the pollutant gases. The crystallite size was about 50 nm with intermediate voids. EDAX analysis confirmed the elemental composition of the films. The films were oxygen-deficient as per EDAX data. NiO3 samples showed the maximum resistivity of 103.13×10^4 Ω·m and a minimum activation energy of 0.3953 eV. The electrical analysis predicted the distinct behavior of the NiO3 sample. The negative value of TCR showed the semiconductor-like behavior of the samples. NiO3 samples showed gas sensitivity of 87% towards the ethanol vapors with good selectivity as compared with the responses towards CO, LPG, NH_3, and NO_2 gases. The oxygen vacancy-based gas sensing mechanism was the probable reason for the improved ethanol vapor sensing. The response time of the sample was 28 s, while the recovery time was 38 s.

Conflict of interest The authors declare no conflict of interest in the publication of the current research article.

References

1. H.Y. Li, L. Huang, X.X. Wang, C.S. Lee, J.W. Yoon, J. Zhou, and J.H. Lee, Molybdenum trioxide nanopaper as a dual gas sensor for detecting trimethylamine and hydrogen sulfide. *RSC Adv.* (2017). https://doi.org/10.1039/c6ra26280e.
2. X. Yin, Y. Guo, H. Xie, W. Que, and L.B. Kong, Nickel oxide as efficient hole transport materials for perovskite solar cells. *Sol. RRL.* (2019). https://doi.org/10.1002/solr.201900001.
3. K. Inzani, M. Nematollahi, F. Vullum-Bruer, T. Grande, T.W. Reenaas, and S.M. Selbach, Electronic properties of reduced molybdenum oxides. *Phys. Chem. Chem. Phys.* (2017). https://doi.org/10.1039/c7cp00644f.
4. S.C. Kulkarni, K.D. Bhalerao, S. Shirse, Y.T. Nakate, U.T. Nakate, B. Pandit, and M.A. Yewale, Screen printed Zn-doped nanostructured In_2O_3 thick films, characterizations, and enhanced NO_2 gas sensing at low temperature. *Ceram. Int.* 48, 29298 (2022). https://doi.org/10.1016/j.ceramint.2022.05.319.
5. B. D. Cullity, Element of x-ray diffraction, 2nd edn. (Addison-Wesley Metallurgy Series,1956)
6. V.V. Deshmane, S. Shinde, G. Jain, and A.V. Patil, Tin modified Fe_2O_3 thick films for monitoring environmental and industrial pollutant gases. *Chem. Africa* 5, 1069 (2022). https://doi.org/10.1007/s42250-022-00398-1.
7. M. Kuźmiński, A. Ślawska-Waniewska, H. Lachowicz, and M. Knobel, The effect of particle size and surface-to-volume ratio distribution on giant magnetoresistance (GMR) in melt-spun Cu–Co alloys. *J. Magn. Magn. Mater.* (1999). https://doi.org/10.1016/s0304-8853(99)00465-5.
8. S. Velliyan and V. Rajendran, Study on the effect of Ce^{3+} doping on structural, morphological and optical properties of CuO nanoparticles synthesized via combustion technique. *Phys. B Condens. Matter* 613, 413015 (2021). https://doi.org/10.1016/j.physb.2021.413015.
9. S.K. Pathak, A. Abate, T. Leijtens, D.J. Hollman, J. Teuscher, L. Pazos, and H.J. Snaith, Towards long-term photo stability of solid-state dye sensitized solar cells. *Adv. Energy Mater.* (2014). https://doi.org/10.1002/aenm.201301667.
10. V.V. Deshmane and A.V. Patil, Study of In2O3 and α-Fe_2O_3 nano-composite as a petrol vapor sensor. *Mater. Res. Exp.* (2018). https://doi.org/10.1088/2053-1591/aaed90.
11. V.V. Deshmane and A.V. Patil, Synergy of semiconductor (Hematite) & catalytic (Ni) properties enhance gas sensing behavior to NO_2. *Mater. Res. Exp.* (2019). https://doi.org/10.1088/2053-1591/ab165e.
12. T.A. Geleta and T. Imae, Nanocomposite photoanodes consisting of p-NiO/n-ZnO heterojunction and carbon quantum dot

additive for dye-sensitized solar cells. *ACS App. Nano Mater.* 4, 236 (2021). https://doi.org/10.1021/acsanm.0c02547.

13. N. Illyaskutty, H. Kohler, T. Trautmann, M. Schwotzer, and V.P.M. Pillai, Enhanced ethanol sensing response from nanostructured MoO_3: ZnO thin films and their mechanism of sensing. *J. Mater. Chem. C* (2013). https://doi.org/10.1039/c3tc30408f.
14. Y. Zhang, P. Chen, Q. Wang, Q. Wang, K. Zhu, K. Ye, and Q. Zhang, High-capacity and kinetically accelerated lithium storage in MoO_3 enabled by oxygen vacancies and heterostructure. *Adv. Energy Mater.* (2021). https://doi.org/10.1002/aenm.202101712.
15. A. Feteira, Negative temperature coefficient resistance (NTCR) ceramic thermistors: an industrial perspective. *J. Am. Ceram. Soc.* (2009). https://doi.org/10.1111/j.1551-2916.2009.02990.x.
16. A.V. Patil, C.G. Dighavkar, S.K. Sonawane, S.J. Patil, and R.Y. Borse, Effect of firing temperature on electrical and structural characteristics of screen printed ZnO thick films. *J. Optoelectron. Biomed. Mater.* 1, 226 (2009).
17. J. Clark, Rate constant and Arrhenius equation. https://www.chemguide.co.uk/physical/basicrates/arrhenius.html, Assessed on 1st May (2022)
18. https://en.wikipedia.org/wiki/Franck%E2%80%93Condon_principle, Assessed on 1st May (2022)
19. V.V. Deshmane and A.V. Patil, Cobalt oxide doped hematite as a petrol vapor sensor. *Mater. Chem. Phys.* (2020). https://doi.org/10.1016/j.matchemphys.2020.122813.
20. R.R. MacLean, G.W. Valentine, P.I. Jatlow, and M. Sofuoglu, Inhalation of alcohol vapor: measurement and implications. *Alcohol. Clin. Exp. Res.* (2017). https://doi.org/10.1111/acer.13291.
21. V. Nadeau, D. Lamoureux, A. Beuter, M. Charbonneau, and R. Tardif, Neuromotor effects of acute ethanol inhalation exposure in humans: a preliminary study. *J. Occup. Health* (2003). https://doi.org/10.1539/joh.45.215.
22. https://www.poison.org/articles/2013-sep/inhaling-alcohol-is-dangerous, Assessed on 1st May (2022)
23. N.J. Dayan, S. Sainkar, R. Karekar, and R. Aiyer, Formulation and characterization of ZnO: Sb thick-film gas sensors. *Thin Solid Films* (1998). https://doi.org/10.1016/s0040-6090(98)00501-x.
24. H.A. Windischmann, Model for the operation of a thin-film SnO [sub x] conductance-modulation carbon monoxide sensor. *J. Electrochem. Soc.* (1979). https://doi.org/10.1149/1.2129098.
25. L. Wang, S. Ma, J. Li, A. Wu, D. Luo, T. Yang, P. Cao, N. Ma, and Y. Cai, Mo-doped SnO_2 nanotubes sensor with abundant oxygen vacancies for ethanol detection. *Sens. Actuators B Chem.* 347, 13062 (2021). https://doi.org/10.1016/j.snb.2021.130642.
26. R.L. Smith and G.S. Rohrer, The protonation of MoO_3 during the partial oxidation of alcohols. *J. Catal.* (1998). https://doi.org/10.1006/jcat.1997.1909.
27. G. Dharmalingam, R. Sivasubramaniam, and S. Parthiban, Quantification of ethanol by metal-oxide-based resistive sensors: a review. *J. Electron. Mater.* 49, 3009 (2020).
28. Y. Zhang, J. Xu, Q. Xiang, H. Li, Q. Pan, and P. Xu, Brush-like hierarchical ZnO nanostructures: synthesis, photoluminescence and gas sensor properties. *J. Phys. Chem. C.* 113, 3430 (2009).
29. G. Niu, C. Zhao, H. Gong, Z. Yang, X. Leng, and F. Wang, NiO nanoparticle-decorated SnO_2 nanosheets for ethanol sensing with enhanced moisture resistance. *Microsyst. Nanoeng.* (2019). https://doi.org/10.1038/s41378-019-0060-7.
30. Y. Mo, Z. Tan, L. Sun, Y. Lu, and X. Liu, Ethanol-sensing properties of α-MoO_3 nanobelts synthesized by hydrothermal method. *J. Alloys Compd.* (2020). https://doi.org/10.1016/j.jallcom.2019.152166.
31. Y. Zhao, S. Wang, X. Zhai, L. Shao, X. Bai, Y. Liu, and Y. Fu, Construction of Zn/Ni bimetallic organic framework derived ZnO/NiO heterostructure with superior N-propanol sensing performance. *ACS Appl. Mater. Interfaces* (2021). https://doi.org/10.1021/acsami.0c21583.
32. J.M. Suh, W. Sohn, Y.S. Shim, J.S. Choi, Y.G. Song, T.L. Kim, and H.W. Jang, p–p heterojunction of nickel oxide-decorated cobalt oxide nanorods for enhanced sensitivity and selectivity toward volatile organic compounds. *ACS Appl. Mater.* (2017). https://doi.org/10.1021/acsami.7b14545.
33. M.H. Raza, K. Movlaee, S.G. Leonardi, N. Barsan, G. Neri, and N. Pinna, Gas sensing of NiO-SCCNT core-shell heterostructures: optimization by radial modulation of the hole-accumulation layer. *Adv. Funct. Mater.* (2019). https://doi.org/10.1002/adfm.201906874.
34. P. Hao, G. Qiu, P. Song, Z. Yang, and Q. Wang, Construction of porous $LaFeO_3$ microspheres decorated with NiO nanosheets for high response ethanol gas sensors. *Appl. Surf. Sci.* (2020). https://doi.org/10.1016/j.apsusc.2020.146025.
35. N. Jayababu, M. Poloju, J. Shruthi, and M.V.R. Reddy, Semi shield driven p-n heterostructures and their role in enhancing the room temperature ethanol gas sensing performance of NiO/SnO_2 nanocomposites. *Ceram.* (2019). https://doi.org/10.1016/j.ceramint.2019.04.255.
36. F. Qu, X. Zhou, B. Zhang, S. Zhang, C. Jiang, S. Ruan, and M. Yang, Fe_2O_3 nanoparticles-decorated MoO_3 nanobelts for enhanced chemiresistive gas sensing. *J. Alloys Compd.* (2019). https://doi.org/10.1016/j.jallcom.2018.12.258.
37. J. Li, H. Liu, H. Fu, L. Xu, H. Jin, X. Zhang, and K. Yu, Synthesis of 1D α-MoO_3/0D ZnO heterostructure nanobelts with enhanced gas sensing properties. *J. Alloys Compd.* (2019). https://doi.org/10.1016/j.jallcom.2019.02.086.
38. U.T. Nakate, R. Ahmad, P. Patil, Y. Wang, K.S. Bhat, T. Mahmoudi, and Y.B. Hahn, Improved selectivity and low concentration hydrogen gas sensor application of Pd sensitized heterojunction n-ZnO/p-NiO nanostructures. *J. Alloys Compd.* (2019). https://doi.org/10.1016/j.jallcom.2019.05.111.
39. N. Kaur, D. Zappa, M. Ferroni, N. Poli, M. Campanini, R. Negrea, and E. Comini, Branch-like NiO/ZnO heterostructures for VOC sensing. *Sens. Actuators B Chem.* (2018). https://doi.org/10.1016/j.snb.2018.02.042.
40. D. Meng, D. Liu, G. Wang, Y. Shen, X. San, M. Li, and F. Meng, Low-temperature formaldehyde gas sensors based on NiO-SnO_2 heterojunction microflowers assembled by thin porous nanosheets. *Sens. Actuators B Chem.* 273, 418 (2018). https://doi.org/10.1016/j.snb.2018.06.030.
41. H. Chen, S. Ao, G.D. Li, Q. Gao, X. Zou, and C. Wei, Enhanced sensing performance to toluene and xylene by constructing $NiGa_2O_4$-NiO heterostructures. *Sens. Actuators B Chem.* (2018). https://doi.org/10.1016/j.snb.2018.11.072.
42. Q. Zhou, W. Zeng, W. Chen, L. Xu, R. Kumar, and A. Umar, High sensitive and low-concentration sulfur dioxide (SO_2) gas sensor application of heterostructure NiO-ZnO nanodisks. *Sens. Actuators B Chem.* (2019). https://doi.org/10.1016/j.snb.2019.126870.
43. C. Su, L. Zhang, Y. Han, C. Ren, M. Zeng, Z. Zhou, and Z. Yang, Controllable synthesis of heterostructured CuO–NiO nanotubes and their synergistic effect for glycol gas sensing. *Sens. Actuators B Chem.* (2019). https://doi.org/10.1016/j.snb.2019.127347.
44. Z. Wang, K. Zhang, T. Fei, F. Gu, and D. Han, α-Fe_2O_3/NiO heterojunction nanorods with enhanced gas sensing performance for acetone. *Sens. Actuators B Chem.* 318, 128191 (2020). https://doi.org/10.1016/j.snb.2020.128191.
45. D. Zhang, Y. Jin, and Y. Cao, Facile synthesis and ammonia gas sensing properties of NiO nanoparticles decorated MoS_2

nanosheets heterostructure. *J. Mater. Sci. Mater. Electron.* (2018). https://doi.org/10.1007/s10854-018-0323-3.

Authors and Affiliations

Dharma K. Halwar[1] · **Vikas V. Deshmane**[2] · **Arun V. Patil**[3]

✉ Arun V. Patil
aruptl@gmail.com

[1] Thick and Thin-Film Laboratory, Department of Electronics, M.S.G. College, Malegaon, Nashik, Maharashtra, India

[2] Department of Physics, SICES Degree College of Arts, Science and Commerce, Ambarnath, Thane, Maharashtra, India

[3] Department of Physics, MGV's Arts, Science, and Commerce College, Manmad, Nashik, Maharashtra, India